Supplementary Information
Low-Temperature Dielectric Anomaly Arising from Electronic Phase Separation at the Mott Insulator-Metal Transition

A. Pustogow*,[1,2] R. Rösslhuber*,[1] Y. Tan*,[3] E. Uykur,[1] A. Böhme,[1] M. Wenzel,[1] Y. Saito,[1,4] A. Löhle,[1] R. Hübner,[1,5] A. Kawamoto,[4] J. A. Schlueter,[6,7] V. Dobrosavljević,[3] and M. Dressel[1]

[1] *1. Physikalisches Institut, Universität Stuttgart, 70569 Stuttgart, Germany*
[2] *Department of Physics and Astronomy, UCLA, Los Angeles, California 90095, U.S.A.*
[3] *National High Magnetic Field Laboratory, Florida State University, Tallahassee, U.S.A.*
[4] *Department of Physics, Hokkaido University, Sapporo, Japan*
[5] *Institut für Klinische Radiologie und Nuklearmedizin, Universität Heidelberg, Mannheim, Germany*
[6] *Material Science Division, Argonne National Laboratory, Argonne, Illinois 60439-4831, U.S.A.*
[7] *Division of Materials Research, National Science Foundation, Alexandria, Virginia 22314, U.S.A.*

CONTENTS

SUPPLEMENTARY NOTE 1: CHARACTERIZATION OF κ-(BEDT-TTF)$_2$Cu$_2$(CN)$_3$ BY PRESSURE AND CHEMICAL SUBSTITUTION

High-quality single crystals of κ-(BEDT-TTF)$_2$Cu$_2$(CN)$_3$ were grown by the standard electrochemical synthesis method [1, 2] at the Universität Stuttgart and Argonne National Laboratory. We measured the complex electrical impedance as a function of pressure, temperature and frequency in order to obtain the permittivity $\hat{\varepsilon} = \varepsilon_1 + \mathrm{i}\varepsilon_2$ or, equivalently, complex conductivity $\hat{\sigma} = \sigma_1 + \mathrm{i}\sigma_2$. To that end, the crystals are contacted by attaching thin gold wires with carbon paint to opposite crystal surfaces, such that the measurements were performed out-of-plane with $E \perp bc$. The experiments were performed with two contacts in a pseudo four-point configuration [3] using an Agilent 4294 impedance analyzer. The applied ac voltage was set to 0.5 V, making sure that we operate in the Ohmic regime. In order to characterize the crystals, we have measured the low-frequency resistivity as a function of temperature and pressure, shown in Supplementary Figure 1.

For pressure-dependent dielectric experiments we utilized a piston-type pressure cell ranging up to approximately 10 kbar with a self-made electrical feedthrough for coaxial cables, which is described in detail in Supplementary Reference 6. Daphne oil 7373 was used as liquid pressure-transmitting medium because it is inert to molecular solids, has a good hydrostaticity, and stays fluid at room temperature for all applied pressures. The inherent pressure loss upon cooling was recorded *in-situ* by an InSb semiconductor pressure gauge that shows a negligible pressure gradient below $T = 50$ K. As a consequence, in the temperature range of particular interest here, the data are collected in the same pressure cycles; this is important for comparison. Unless indicated otherwise, throughout the manuscript we state the pressure reading at $T = 10$ K.

The pressure cell was cooled down in a custom-made continuous-flow helium cryostat that allows us to reduce the total cable length to 50 cm enabling reliable measurements at frequencies up to 5 MHz. The compact cryostat design results in a rather steep thermal gradient limiting the lowest reachable temperature to about 8 K. No dependence on the cooling rate was observed, which was kept below 0.4 K/min for all measurements. Performing similar experiments on different single crystals yields good agreement with the results presented here.

Supplementary Figure 1 displays the out-of-plane resistivity $\rho_1(T)$ curves probed at low frequency. The indicated pressure values were recorded at $T = 10$ K. Although these are two-point measurements, the results are in good

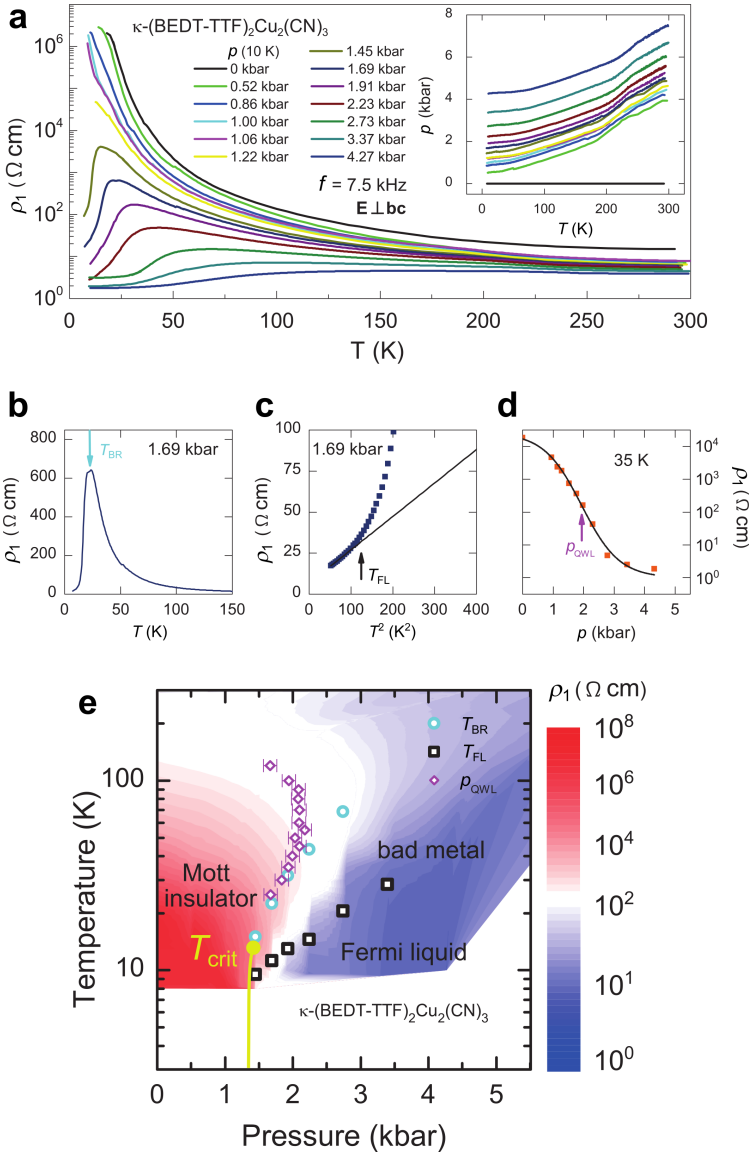

Supplementary Figure 1. **a,** Temperature-dependent out-of-plane resistivity $\rho_1(T)$ of κ-(BEDT-TTF)$_2$Cu$_2$(CN)$_3$ for sample 2 under hydrostatic pressure, measured along the a-direction and at $f = 7.5$ kHz, which is in good agreement with dc-measurements known from literature [4, 5]. With increasing pressure, $\rho_1(T)$ is reduced, revealing the insulator-metal transition for $p > 1.45$ kbar. The inset in panel **a** displays the *in-situ* measured pressure loss upon cooling. **b,** The maximum in $\rho_1(T)$ (cyan arrow) directly indicates the onset of metallic conduction at the Brinkman-Rice temperature $T_{\rm BR}$. **c,** We define $T_{\rm FL}$ as the temperature at which ρ_1 deviates from $\rho_{1,\rm FL} = \rho_0 + AT^2$ by more then 10%. **d,** The quantum Widom line is determined by fitting $\rho_1(p)$ (orange squares) at constant temperature with $\log(\rho_{1,\rm QWL}) = c[1 - \tanh\{b(p - p_{\rm QWL})\}]$ (black line). **e,** Phase diagram which is based on a contour plot of $\rho_1(p, T)$, including $T_{\rm max}$, $T_{\rm FL}$ and $p_{\rm QWL}$. The yellow line represents an estimate of the Mott transition with a critical end point at $T_{\rm crit} = 16$ K and $p_{\rm crit} = 1.45$ kbar.

agreement with the four-point dc-measurements reported in literature [4, 5], taking into account that we probe the perpendicular direction. For both samples we observe a maximum in $\rho_1(T)$ that shifts to higher T with increasing pressure; concomitantly the resistivity is reduced.

The resistivity maximum at the Brinkman-Rice temperature $T_{\rm BR}$ indicates the onset of the metallic transport regime with $\mathrm{d}\rho_1/\mathrm{d}T < 0$. The Fermi-liquid regime is characterized by $\rho_1(T) = \rho_0 + AT^2$. We define $T_{\rm FL}$ as the temperature where $\rho_1(T)$ deviates by more than 10% from this quadratic behavior. We remind here, that the experimental setup did not allow for cooling below 8 K such that the superconducting state below $T_{\rm SC} = 4$ K could not be reached.

The inset in Supplementary Figure 1a shows the decrease of the *in-situ* recorded pressure upon cooling. The step like features around 220 K correspond to the solidification temperature of the pressure transmitting oil. Below 50 K,

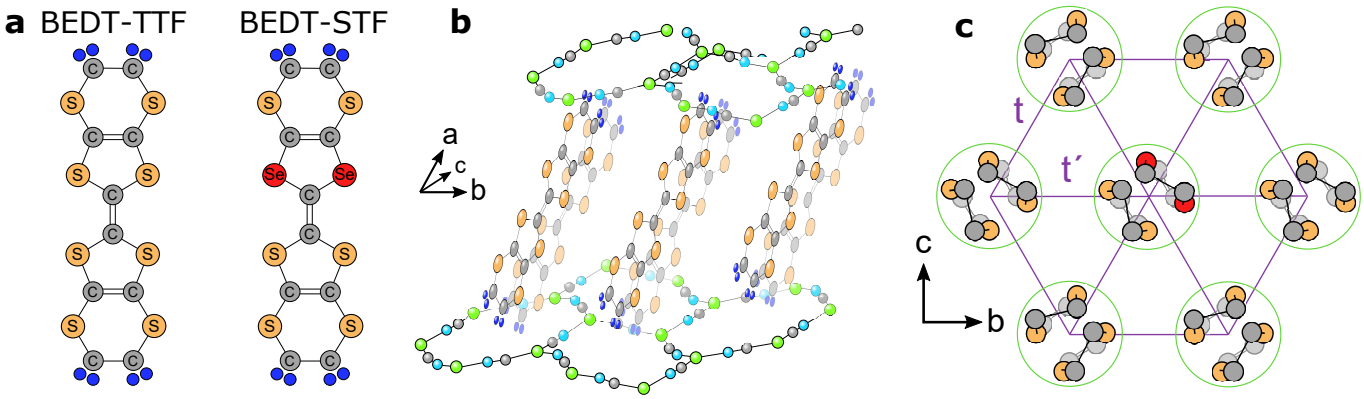

Supplementary Figure 2. **a,** Organic donor molecules bis-(ethylenedithio)-tetrathiafulvalene, called BEDT-TTF, and bis-(ethylenedithio)-diseleniumdithiafulvalene, abbreviated BEDT-STF. In the latter case two sulfur atoms of the inner rings are replaced by selenium. **b,** The crystal structure contains dimers of the donor molecules forming layers in the *bc*-plane which are separated by the $Cu_2(CN)_3$ anion sheets. **c,** The dimers are arranged in a triangular pattern with transfer integrals $t'/t = 0.83$ [10] close to complete frustration. The STF-substitution leads to a spatially random extension of the transfer integrals due to the larger molecular orbitals.

the pressure saturates and becomes nearly temperature-independent. For the 0 kbar measurement, the sample was cooled in the pressure cell, which was left open, only filled with He contact gas, such that pressure loss upon cooling is negligible.

The precise *in-situ* measurement of $p(T)$ enables us to analyze $\rho_1(p)$ at constant temperature. In particular, we determine the quantum Widom line (QWL) by fitting $\rho_1(p)$ (orange squares) at constant temperature with $\log\{\rho_1\} = c[1-\tanh\{b(p-p_{\mathrm{QWL}})\}]$ (black line), as examplarily shown in Supplementary Figure 1d. This procedure [7, 8] yields the QWL as the point of inflection at p_{QWL} which is indicated by the magenta arrow.

κ-[(BEDT-STF)$_x$(BEDT-TTF)$_{1-x}$]$_2$Cu$_2$(CN)$_3$ single crystals with varying stoichiometry (x = 0, 0.04, 0.1, 0.12, 0.16, 0.19, 0.21, 0.25, 0.28, 0.44, 0.78 and 1) were prepared by standard electrochemical oxidation [1]. Both BEDT-TTF and BEDT-STF (molecules displayed in Supplementary Figure 2a) were synthesized at Hokkaido University in Sapporo, where also the crystal growth is carried out. For the alloying series, the amount of donor molecules was preselected; for each batch the actual substitution value x was determined *a posteriori* by energy-dispersive x-ray spectroscopy: using κ-(BEDT-TTF)$_2$Cu$_2$(CN)$_3$ as a reference we compared the intensity of S atoms to that of Se atoms [9]. The structure consists of *bc* layers of strongly dimerized BEDT-TTF or BEDT-STF molecules, with each dimer oriented approximately perpendicular to its nearest neighbors (Supplementary Figure 2b,c).

Electrical transport was measured parallel to the *c*-axis from room temperature down to $T = 1.8$ K by the standard four-probe technique. For this, thin gold wires were contacted by carbon paste. Furthermore, we measured the complex electrical impedance as a function of temperature and frequency in order to obtain the dielectric permittivity $\hat{\varepsilon} = \varepsilon_1 + \mathrm{i}\varepsilon_2$. Here, gold wires were attached to opposite crystal surfaces and the data recorded by an impedance analyzer in the frequency range from 40 Hz to 10 MHz covering temperatures down to $T = 5$ K. The applied ac voltage was set to 0.5 V, making sure that we operate in the Ohmic regime.

Supplementary Figure 3 displays the *c*-axis dc resistivity $\rho(T)$ as a function of temperature for all samples in our substitution series from $x = 0$ to 1. The room-temperature values increase from approximately 0.03 Ωcm for $x = 1$ to around 0.5 Ωcm for $x = 0$. For $x = 0.12$ and higher the system turns metallic at low temperatures; the range of metallic conductivity below the Brinkman-Rice temperature T_{BR} increases for larger substitution and exceeds $T = 300$ K for $x \geq 0.44$. For very low temperatures, the metallic properties are clearly characterized by a $\rho(T) \propto T^2$ behavior that is the hallmark of electron-electron interaction. A detailed analysis of the Fermi-liquid properties will be provided elsewhere.

SUPPLEMENTARY NOTE 2: DIELECTRIC RESPONSE AS A FUNCTION OF PRESSURE

In order to give an overview on the temperature-dependent dielectric response of κ-(BEDT-TTF)$_2$Cu$_2$(CN)$_3$ in the various regimes, in Supplementary Figure 4 we plot the real part of the dielectric permittivity $\varepsilon_1(T)$ for selected frequencies and pressures as indicated. Starting from ambient conditions, a pronounced peak dominates the temperature

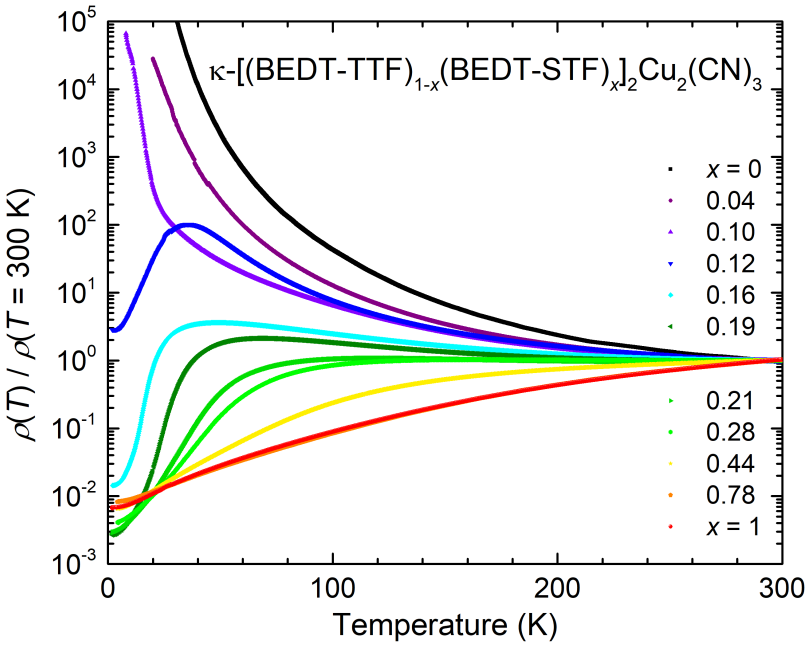

Supplementary Figure 3. Temperature dependence of the dc resistivity of κ-[(BEDT-STF)$_x$(BEDT-TTF)$_{1-x}$]$_2$Cu$_2$(CN)$_3$ for various substitution values x as indicated spanning the full range from the insulating $x = 0$ to the metallic side. The data are measured along the highly conducting c-axis and normalized to the respective room-temperature value for better comparison.

dependence of the dielectric constant. The maximum shifts to lower temperatures as pressure increases (Supplementary Figure 4a-e) and, exceeding $p = 1.22$ kbar, it moves out of the accessible temperature window. Most important, however, are the drastic changes of the dielectric response around the insulator-metal transition at $p_{\rm IMT} = 1.45$ kbar [5]. For $p = 1.45$ up to 2.2 kbar, ε_1 is strongly enhanced for $T < 20$ K with a frequency-dependent amplitude even exceeding 10^5 at $f = 7.5$ kHz (Supplementary Figure 4f-h). As pressure increases further, the onset of the dielectric anomaly shifts to higher temperatures, reaching about 30 K at $p = 2.23$ kbar, for instance (Supplementary Figure 4h). We ascribe this observation to a coexistence region centered around the Mott insulator-metal transition (IMT), where spatially segregated metallic regions in an insulating matrix grow in a percolative manner. At $p = 3.37$ kbar and higher (Supplementary Figure 4i,j), ε_1 becomes negative and large for nearly all frequencies indicating purely metallic behavior.

The most surprising observation of Supplementary Figure 4 is the dramatic increase of the dielectric constant of κ-(BEDT-TTF)$_2$Cu$_2$(CN)$_3$ for $p > 1.2$ kbar. In Supplementary Figure 5 we plot the pressure dependence of $\varepsilon_1(p)$ and $\sigma_1(p)$ as obtained for a fixed frequency of $f = 100$ kHz at different temperatures; Fig. 3a,b of the main paper displays a similar data set recorded at 380 kHz. A pronounced peak in the permittivity appears around 1.8 kbar followed by a drop to negative values evidencing the onset of metallic conduction. We explain this observation by percolation when the insulator-metal phase boundary is approached: metallic puddles develop within the insulating matrix and grow with increasing pressure.

At the lowest temperature, $T = 10$ K, the peak maximum occurs at a pressure slightly above $p_{\rm IMT}$. This can be understood when recalling the definition of the percolation threshold as the first continuous conducting path, while the dielectric constant is integrated over the entire volume; hence the overall capacitance still increases even when some inclusions already coalesce. As seen from Supplementary Figure 5a, the peak in $\varepsilon_1(p)$ shifts to even higher pressure values as T rises, but strongly diminishes upon heating; for $T > 22$ K the anomaly is completely suppressed. Eventually, a simple drop in permittivity remains with a change in sign to large negative values of $\varepsilon_1(p = 4.3\ \text{kbar}) \approx -10^3$ to -10^4.

The enhancement of the dielectric constant is accompanied by a step-like feature in the conductivity, presented in Supplementary Figure 5b. With pressure, the metallic fraction grows; consequently $\sigma_1(p)$ rises continuously until it saturates in the metallic phase where the pressure-dependence of the conductivity is minuscule. The inflection point corresponds to $p_{\rm IMT}$, defined above by dc-resistance measurements [5]. With rising temperature, the step feature shifts to higher pressure values, smears out and becomes a more gradual increase consistent with the change from the first-order IMT to the crossover region upon heating through $T_{\rm crit}$.

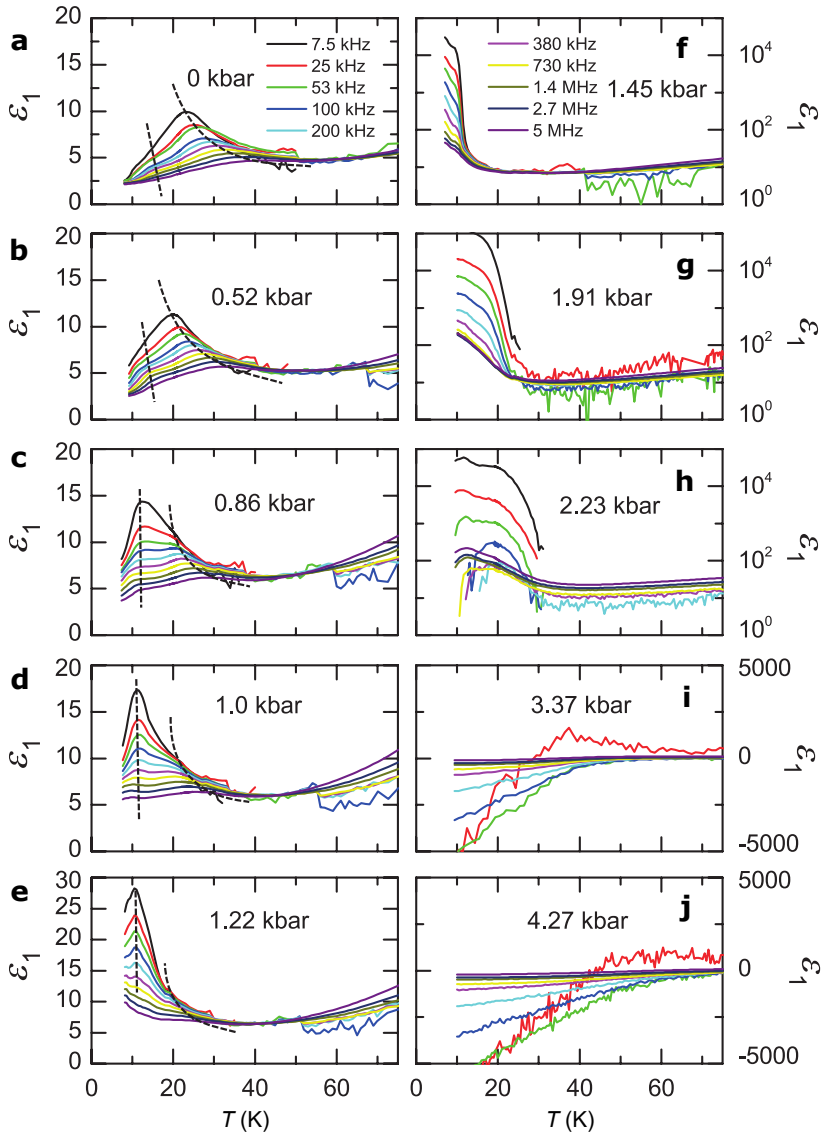

Supplementary Figure 4. Plot of the dielectric permittivity $\varepsilon_1(T)$ of κ-(BEDT-TTF)$_2$Cu$_2$(CN)$_3$ for several frequencies from 7.5 kHz to 5 MHz upon increasing pressure. Note the different ordinates used in the various panels. **a,** At $p = 0$ kbar and below $T = 50$ K, we observe a relaxor-type ferroelectric peak with shrinking amplitude that shifts to higher temperature with increasing frequency. **b-e,** Additionally, a shoulder-like feature is revealed at ambient pressure around $T = 15$ K which develops into a second peak upon pressurization. **f-h,** In the coexistence phase between $p = 1.45$ and 2.23 kbar, an enormous increase of ε_1 is observed which is strongly frequency-dependent and attributed to spatially separated metallic and insulating regions. **i,j,** Above $p = 3.37$ kbar, $\varepsilon_1 < 0$ for nearly all measured frequencies indicating metallic behavior.

The dielectric properties of percolating systems have been subject of numerous investigations for half a century [11, 12]. As pointed out by Efros and Shklovskii [13] the static dielectric constant of a percolating system is a function of the filling fraction m of the metallic phase and diverges at the percolation threshold in the limit $T \to 0$ and $\omega \to 0$. The divergency gets reduced and rounded as the insulating matrix acquires a finite conductivity σ_i, for instance as temperature rises:

$$\varepsilon_1(T, m_c) \propto \left[\frac{\sigma_m(T)}{\sigma_i(T)}\right]^{1-s} \quad , \tag{1}$$

where $s = 0.5$ and 0.62 in two and three dimensions, respectively [13], and σ_m denotes the conductivity of the metallic regions. Although our data do not permit a quantitative comparison, the observed reduction of the peak seen in Supplementary Figure 5a is in accord with the tendency of Eq. (1).

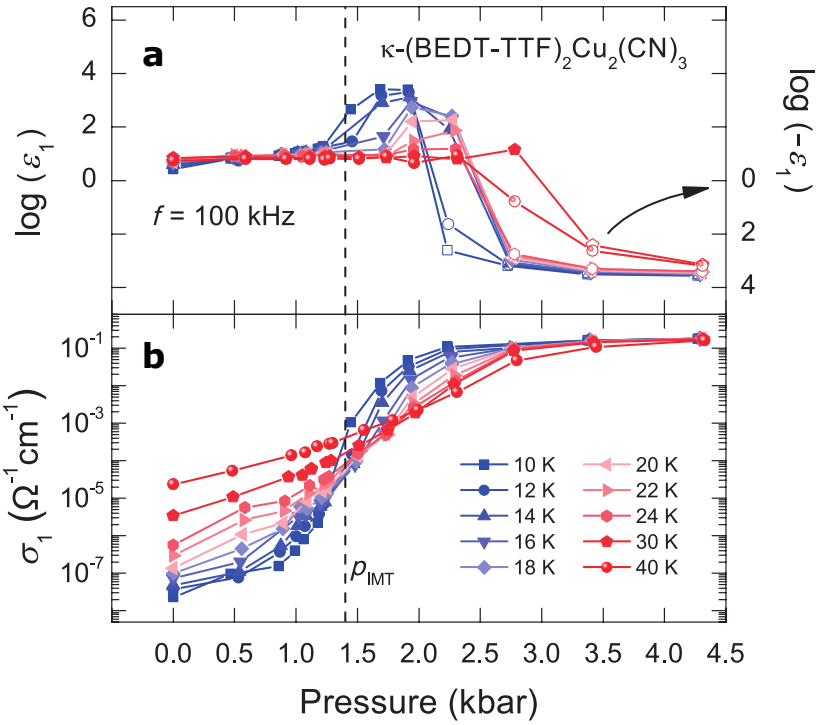

Supplementary Figure 5. Pressure dependence of the dielectric properties of κ-(BEDT-TTF)$_2$Cu$_2$(CN)$_3$ recorded at different temperatures for a fixed frequency $f = 100$ kHz. **a,** The permittivity ε_1 forms a pronounced maximum followed by a rapid drop to negative values. **b,** The conductivity σ_1 exhibits a step-like increase with an inflection point located right at the onset of the peak in ε_1. This percolating behavior stems from the nucleation and growth of metallic puddles spatially separated in an insulating matrix; the filling fraction increases by applying pressure. With rising temperature the features shift to higher pressures and diminish in amplitude and step size, respectively.

Alternatively, at $T = 0$ ($\sigma_i = 0$) and for $m = m_c$ one expects a reduction of the peak amplitude when probed at finite frequencies, according to [13]

$$\varepsilon_1(\omega, m_c) \propto (1/\omega)^{1-s} \quad . \tag{2}$$

Choosing the pressure for which the dielectric constant reaches the maximum value, in Supplementary Figure 6 we plot the frequency-dependence of $\varepsilon_1(\omega, p = 1.7$ kbar) for several temperatures. For $T \leq 16$ K, $\varepsilon_1(\omega)$ strongly drops with increasing frequency following a power-law for two orders of magnitude before it levels off at $f_0 = \omega/(2\pi) \approx 2$ MHz. In the vicinity of the critical endpoint and above $T_{\rm crit}$, the percolative behavior vanishes and merges into a frequency-independent response. Following Eq. (2), we fit the data in Supplementary Figure 6 and obtain an exponent $1 - s$ for each temperature, displayed in the inset. The deviation from theory has several reasons: standard percolation theory does not take into account field enhancement effects between adjacent finite metallic clusters beyond the dipole approximation and/or hopping of charge carriers between them as well as electron-electron interactions, as pointed out previously [14–17]. Sarychev and Brouers [18] explicitly account for tunneling between finite metallic clusters in order to explain the low-frequency response of percolating systems.

SUPPLEMENTARY NOTE 3: DIELECTRIC RESPONSE AS A FUNCTION OF CHEMICAL SUBSTITUTION

In a first approach, the dielectric properties in the infrared spectral range can be obtained from optical reflectivity data (not shown) as a function of frequency, temperature and substitution. Supplementary Figure 7 displays the real part $\varepsilon_1(\omega)$ for the different κ-[(BEDT-STF)$_x$(BEDT-TTF)$_{1-x}$]$_2$Cu$_2$(CN)$_3$ crystals recorded at $T = 5$ K. In the Mott-insulating state ($x \leq 0.1$), the permittivity is basically frequency-independent and acquires a small, positive value. As x increases, the quasi-static $\varepsilon_1(\omega \to 0)$ first increases before it rapidly drops to large negative values. After crossing the Mott insulator-metal transition the system becomes conductive: the strong screening of the coherent

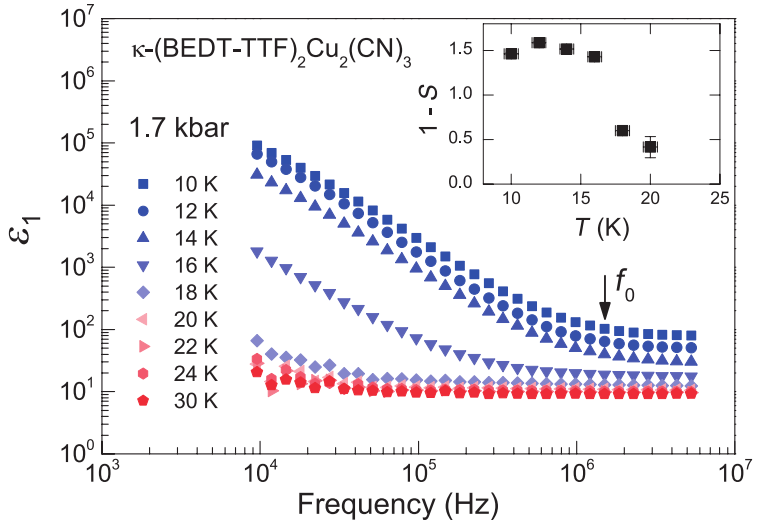

Supplementary Figure 6. Double-logarithmic plot of $\varepsilon_1(f)$ at 1.7 kbar for various temperatures, as indicated. For $T \leq 16$ K a power-law behavior is observed, which saturates above $f_0 \approx 2$ MHz. The percolating behavior of κ-(BEDT-TTF)$_2$Cu$_2$(CN)$_3$ is suppressed for $T > 16$ K where the first-order transition becomes a gradual crossover. The inset shows the temperature dependence of the exponent $1 - s$ obtained from fits by Eq. (2).

quasiparticles drives ε_1 negative. A similar observation was reported for the Mott transition of VO_2, where the low-frequency permittivity diverges as a function of temperature. Near-field optical microscopy revealed that this behavior stems from the phase coexistence of metallic puddles in an insulating matrix [19]. In general, the divergency of the dielectric permittivity $\varepsilon_1(x)$ is a hallmark of percolative phase transitions in microemulsions [20–24], composites [25–27] or percolating metal films [28–32].

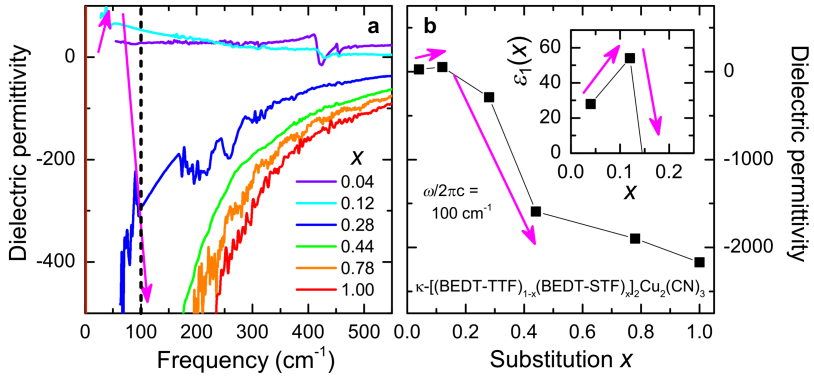

Supplementary Figure 7. Despite continuously increasing low-frequency conductivity, in the low-frequency limit the dielectric permittivity $\varepsilon_1(x)$ exhibits a peak around the Mott transition, reminiscent of a percolative-type coexistence of metallic and insulating regions. **a,** Real part of the dielectric permittivity $\varepsilon_1(x)$ as obtained from far-infrared reflectivity measurements for $E \parallel c$ at $T = 5$ K for κ-[(BEDT-STF)$_x$(BEDT-TTF)$_{1-x}$]$_2$Cu$_2$(CN)$_3$ with various substitutions x as indicated. **b,** To better follow the substitutional dependence, we display the dielectric permittivity taken at $\omega/(2\pi c) = 100$ cm^{-1} – corresponding to 3.3 THz – indicated by the dashed line in panel **a**.

Since audio- and radio-frequency experiments are more suitable for exploring the dielectric behavior at the insulator-metal transition, we have conducted dielectric experiments down to 7.5 kHz. Supplementary Figure 8 summarizes the dielectric response of κ-(BEDT-TTF)$_2$Cu$_2$(CN)$_3$ and how it is affected by moving across the Mott insulator-to-metal transition via STF-substitution. We plot the real part of the permittivity ε_1 as a function of temperature T for selected frequencies f and substitutions x, as indicated. The pronounced peak dominating the temperature dependence of $\varepsilon_1(T)$ was discovered by Abdel-Jawad *et al.* [33] and subsequently confirmed by other groups [34–37]. When probed at $f = 7.5$ kHz, the maximum is observed around $T = 30$ K in the case of κ-(BEDT-TTF)$_2$Cu$_2$(CN)$_3$ (Supplementary Figure 8a); with a slight sample-to-sample dependence, in agreement with previous reports. The peak shifts to higher

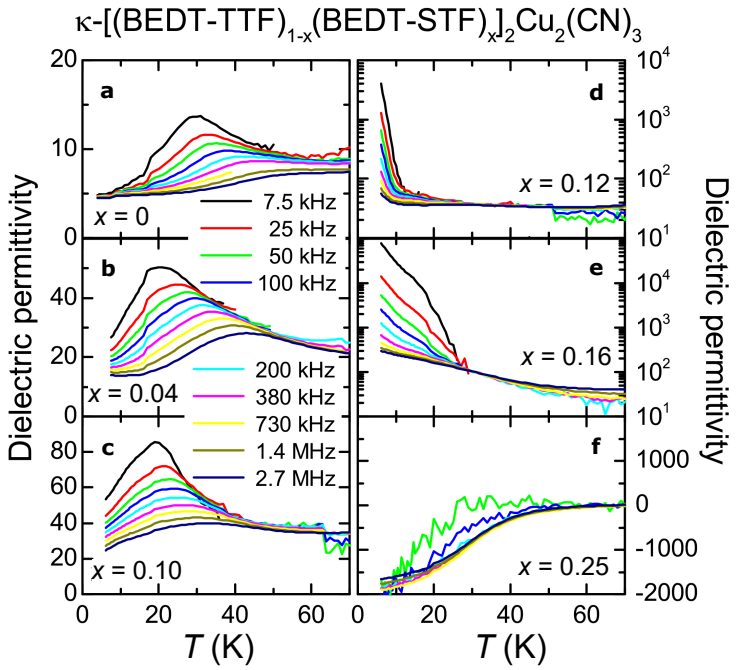

Supplementary Figure 8. Temperature-dependent dielectric permittivity of κ-[(BEDT-STF)$_x$(BEDT-TTF)$_{1-x}$]$_2$Cu$_2$(CN)$_3$ for substitutional values $x = 0$, 0.04, 0.10, 0.12, 0.16 and 0.25 measured at several frequencies. Note the different ordinates used in the various panels. **a,** The pure crystal exhibits a relaxor-type ferroelectric feature below $T = 50$ K, which becomes more pronounced and shifts to lower T as frequency gets smaller. **b,c,** As x is increased to 0.1, $\varepsilon_1(T)$ rises strongly and the peak appears at lower temperatures. **d,e,** Eventually the permittivity reaches values of 10^5 due to the coexistence of spatially separated metallic and insulating regions. The response is strongly frequency dependent. **f,** Upon percolation around $x = 0.2$, the dielectric constant is negative, giving evidence for the metallic behavior that continues for all higher substitutions up to $x = 1$.

temperatures as the frequency increases; at the same time, however, it gets less pronounced. This behavior resembles the well-known phenomenology of relaxor ferroelectrics [38].

Already the minimal substitution of $x = 0.04$ and 0.1 enhances the dielectric permittivity significantly with the maximum $\varepsilon_1(f = 7.5\text{ kHz}) \approx 50$ and 80. This strong increase of $\varepsilon_1(T)$ and concomitant shift of the peak to lower temperatures when we approach the insulator-metal transition is in full accord with our pressure-dependent dielectric studies in Supplementary Note 2, where an extensive and detailed analysis is given. As we approach the phase transition further ($x = 0.12$ and 0.16), the dielectric constant drastically diverges, reaching values up to 10^5 in the static low-temperature limit. A divergency in $\varepsilon_1(x)$ is the fingerprint of a percolative phase transition where metallic regions form in an insulating matrix [11, 13, 39]. When crossing the percolation threshold, the system acts like a metal, characterized by a negative dielectric permittivity, $\varepsilon_1 < 0$. With rising x the sign change of the dielectric constant traces the Brinkman-Rice temperature, as it was identified by the maximum in $\rho(T)$ (Supplementary Figure 3) [40]. These results confirm the observations we extracted from the optical response in Supplementary Figure 7.

SUPPLEMENTARY NOTE 4: THEORETICAL ANALYSIS OF THE DIELECTRIC PERMITTIVITY AT THE IMT

The dielectric properties of a mixture of spatially segregated conductive and insulating regions are commonly modelled by Bruggeman's effective medium approach [11, 41–43]:

$$m\,\frac{\varepsilon_m - \varepsilon_{\text{eff}}}{\varepsilon_{\text{eff}} + L(\varepsilon_m - \varepsilon_{\text{eff}})} + (1-m)\,\frac{\varepsilon_i - \varepsilon_{\text{eff}}}{\varepsilon_{\text{eff}} + L(\varepsilon_i - \varepsilon_{\text{eff}})} = 0 \quad , \tag{3}$$

where m is the volume fraction of the metallic inclusions, L is the shape factor, ε_i and ε_{m} are the complex permittivities of the insulating and metallic phases, respectively, and ε_{eff} is the effective permittivity of the composite. In the following, we determine the complex dielectric response on purely theoretical ground. To that end, we calculate

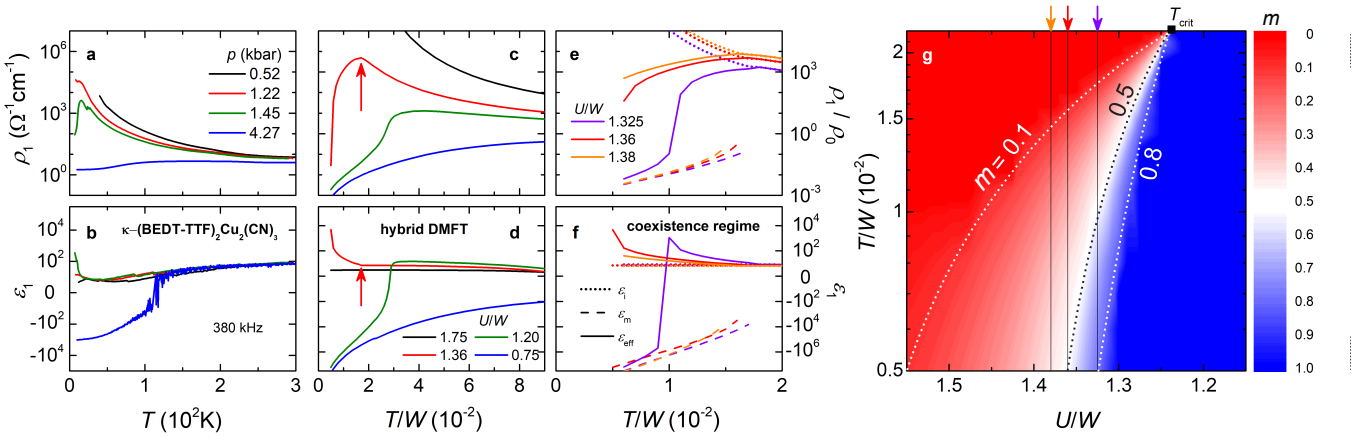

Supplementary Figure 9. **a,b,** Pressure evolution of the temperature-dependent resistivity and permittivity measured at $f = 380$ kHz along the a-axis of κ-(BEDT-TTF)$_2$Cu$_2$(CN)$_3$. **c,d,** Calculated resistivity and permittivity using hybrid DMFT with different strength of effective correlations U/W as indicated. The red arrows indicate the temperature below which the coexistence regime is entered. **e,f,** For selected values of U/W close to the Mott insulator-metal transition the temperature-dependent resistivity and permittivity are plotted for the insulating phase, ε_i (dotted lines), the metallic phase ε_m (dashed lines) and the resulting effective medium $\varepsilon_{\rm eff}$ (solid lines) at lowest temperatures in the coexistence regime. **g,** Volume fraction m of the metallic component in a false-color presentation according to the right scale. The dependence on correlation strength U and temperature T, normalized to the bandwidth W, is calculated by Eq. (6). The dotted lines represent $m = 0.1$, 0.5 and 0.8. Since in our model $L = \frac{1}{2}$, the metallic domains stop connecting at $m = 0.5$; here the conductivity drops sharply. The black solid lines indicate the effective correlation strength used for calculating the temperature dependence of $\rho_1(T)$ and $\varepsilon_1(T)$ shown in panels **e** and **f** by purple, red and orange colors.

$\varepsilon_m(\omega, T)$ and $\varepsilon_i(\omega, T)$ of the pure metallic and insulating phases and use them to obtain the electrodynamic properties of the mixture via Eq. (3) by utilizing a phenomenological model for the metallic filling fraction. We assume a half-filled Hubbard model in two dimensions with semicircular bands and apply dynamical mean-field theory (DMFT) calculations. Within the single site DMFT approach, the real part of optical conductivity $\sigma_1(\omega)$ is given by the expression [44–46]

$$\begin{aligned}\sigma_1(\omega) = &\frac{2e^2}{\pi\hbar}\frac{1}{a}\frac{1}{S}\int \mathrm{d}E\,\rho_0(E)\,[V(E)]^2 \\ &\times \int_{-\infty}^{+\infty}\mathrm{d}(\hbar\nu)\frac{f(\hbar\nu)-f(\hbar\nu+\hbar\omega)}{\hbar\omega} \\ &\times \mathrm{Im}\,\{G(\hbar\nu+\hbar\omega,E)\}\,\mathrm{Im}\,\{G(\hbar\nu,E)\}\,,\end{aligned} \tag{4}$$

where

$$G(\hbar\nu, E) = \frac{1}{\hbar\nu - E - \Sigma(\hbar\nu)},$$

is the Green function and $\Sigma(\hbar\nu)$ is the local self energy. The imaginary part of the optical conductivity $\sigma_2(\omega)$ is then calculated via Kramers-Kronig transform [45]:

$$\sigma_2(\omega) = -\frac{2}{\pi}\int_0^\infty \frac{\omega\sigma_1(\omega')}{\omega'^2-\omega^2}\mathrm{d}\omega' \quad . \tag{5}$$

Applying these expressions (4) and (5), we obtain the complex dielectric response $\hat{\varepsilon}(\omega) = 1 + \mathrm{i}\hat{\sigma}(\omega)/(\omega\varepsilon_0)$, via DMFT across the entire phase diagram, as a function of temperature T and the interaction U. We stress that within the coexistence region we find two locally stable solutions, while outside there is only one solution. In Eq. (4), $a = 15$Å, is the distance between layers for our material [1], yielding a sheet conductance $e^2/(ha) \approx 260\ (\Omega\mathrm{cm})^{-1}$. $V(E)/\sqrt{S}$ is the current vertex, which is equal to $\sqrt{(D^2-E^2)/3}$, and $\rho_0(E) = 2\sqrt{D^2-E^2}/\pi D^2$ is the semicircular model density of states of non-interacting electrons of bandwidth $W = 2D$.

In order to calculate the total dielectric function within the (percolating) coexistence region, we not only have to know the dielectric function for each of the two phases, ε_i and ε_m, but also the relative volume fraction of the

two components as a function of temperature T and effective correlations U/W. For simplicity, we use a hyperbolic tangent function to represent the metallic volume fraction m:

$$m\left(\frac{T}{W},\frac{U}{W}\right)=\frac{1}{2}\tanh\left\{\frac{c\left[(U/W)_{\mathrm{crit}}-(U/W)\right]}{(T/W)_{\mathrm{crit}}-T/W}\right\}+\frac{1}{2}, \tag{6}$$

which is centered around $(U/W)_{\mathrm{crit}}=(0.20-T/W)/0.14$, as depicted in Supplementary Figure 9g. We also select $c=0.1$ for $U/W>(U/W)_{\mathrm{crit}}$ and $c=0.3$ for $U/W>(U/W)_{\mathrm{crit}}$ in order to mimic the experimental findings.

Finally, we obtain the optical conductivity $\sigma_1(\omega,T)$ and dielectric permittivity $\varepsilon_1(\omega,T)$ inside the coexistence region via the BEMA Eq. (3). We assumed $L=\frac{1}{2}$ for our calculations, but the findings can be easily scaled to $L=\frac{1}{3}$. Here we focus on very low frequency $\omega/(2\pi)=5\cdot10^{-9}W\approx320$ kHz, in order to allow comparison of the calculated permittivity with our experiments. For better relating our calculated to experimental results, in Supplementary Figure 9 we plot representative curves of electrical resistivity $\rho_1(T)$ and dielectric permittivity $\varepsilon_1(T)$ for various correlation strengths U covering the insulating, percolating and metallic regions of the phase diagram. For large U/W the system behaves insulating with a small positive dielectric constant, corresponding to the behavior observed at ambient and low pressure ($p<1$ kbar). For intermediate correlation strength $U/W=1.36$, the resistivity starts insulating at high temperatures, but $\rho_1(T)$ exhibits a maximum around $T/W\approx1.6$ below which it turns weakly metallic. Upon cooling, the system enters the coexistence regime with metallic inclusions, as depicted in Supplementary Figure 9g. Around that temperature, $\varepsilon_1(T)$ rises rapidly, acquiring 10^4 near the percolation threshold. This temperature dependence resembles the observations on κ-(BEDT-TTF)$_2$Cu$_2$(CN)$_3$ for $p=1.45$ kbar. As U/W decreases further, the phase boundary to the metallic phase is crossed with a drop in $\rho_1(T)$ and a sign change in the dielectric constant. For $U/W=1.75$ metallic properties are found in the entire temperature range. This behavior is reached for the highest pressure values above 4 kbar. The full set of data is presented in Figs. 1 and 4.

Here we want to focus on the regime right at the IMT and therefore plot the behavior for U/W close to the critical correlation strength. In Supplementary Figure 9e,f the properties $\rho_1(T)$ and $\varepsilon_1(T)$ of the constituting insulating and metallic phases are plotted together with the effective behavior $\varepsilon_{\mathrm{eff}}$. The coexistence regime is entered around $T/W=0.016$ to 0.018 – the particular value depends on the effective correlations U/W according to Eq. (6) – and there the resistivity drops, accompanied by a change in sign of the dielectric constant to large negative values due to screening in the metal. For $U/W=1.325$ the metallic state is reached at significantly lower temperatures, as seen in Supplementary Figure 9g.

Supplementary References

[1] Geiser, U. *et al.* Superconductivity at 2.8 K and 1.5 kbar in κ-(BEDT-TTF)$_2$Cu$_2$(CN)$_3$: The first organic superconductor containing a polymeric copper cyanide anion. *Inorg. Chem.* **30**, 2586–2588 (1991).

[2] Komatsu, T., Matsukawa, N., Inoue, T. & Saito, G. Realization of superconductivity at ambient pressure by band-filling control in κ-(BEDT-TTF)$_2$Cu$_2$(CN)$_3$. *J. Phys. Soc. Jpn.* **65**, 1340–1354 (1996).

[3] Keysight technologies. *Impedance measurement handbook*, 6 Edn. (2009).

[4] Kurosaki, Y., Shimizu, Y., Miyagawa, K., Kanoda, K. & Saito, G. Mott transition from a spin liquid to a Fermi liquid in the spin-frustrated organic conductor κ-(ET)$_2$Cu$_2$(CN)$_3$. *Phys. Rev. Lett.* **95**, 177001 (2005).

[5] Furukawa, T., Kobashi, K., Kurosaki, Y., Miyagawa, K. & Kanoda, K. Quasi-continuous transition from a Fermi liquid to a spin liquid in κ-(ET)$_2$Cu$_2$(CN)$_3$. *Nat. Commun.* **9**, 307 (2018).

[6] Rösslhuber, R., Uykur, E. & Dressel, M. Pressure cell for radio-frequency dielectric measurements at low temperatures. *Rev. Sci. Instr.* **89**, 054708 (2018).

[7] Pustogow, A. *et al.* Quantum spin liquids unveil the genuine Mott state. *Nat. Mater.* **17**, 773–777 (2018).

[8] Furukawa, T., Miyagawa, K., Tanigchi, H., Kato, R. & Kanoda, K. Quantum criticality of Mott transition in organic materials. *Nat. Phys.* **11**, 221–224 (2015).

[9] Saito, Y., Minamidate, T., Kawamoto, A., Matsunaga, N. & Nomura, K. Site-specific ^{13}C nmr study on the locally distorted triangular lattice of the organic conductor $\kappa-(\mathrm{BEDT-TTF})_2\mathrm{Cu}_2(\mathrm{CN})_3$. *Phys. Rev. B* **98**, 205141 (2018).

[10] Kandpal, H. C., Opahle, I., Zhang, Y.-Z., Jeschke, H. O. & Valentí, R. Revision of model parameters for κ-type charge transfer salts: An ab initio study. *Phys. Rev. Lett.* **103**, 067004 (2009).

[11] Kirkpatrick, S. Percolation and conduction. *Rev. Mod. Phys.* **45**, 574–588 (1973).

[12] Shklovskii, B. I. & Efros, A. L. *Electronic properties of doped semiconductors* (Springer-Verlag, Berlin, 1984).

[13] Efros, A. L. & Shklovskii, B. I. Nonmonotonic relaxation kinetics of confined systems. *Phys. Stat. Sol. (b)* **76**, 475 (1976).

[14] Laibowitz, R. B. & Gefen, Y. Dynamic scaling near the percolation threshold in thin Au films. *Phys. Rev. Lett.* **53**, 380–383 (1984).

[15] Hundley, M. F. & Zettl, A. Temperature-dependent ac conductivity of thin percolation films. *Phys. Rev. B* **38**, 10290–10296 (1988).

[16] Yoon, C. S. & Lee, S.-I. Measurements of the ac conductivity and dielectric constant in a two-dimensional lattice percolation system. *Phys. Rev. B* **42**, 4594–4597 (1990).

[17] Pakhomov, A. B., Wong, S. K., Yan, X. & Zhang, X. X. Low-frequency divergence of the dielectric constant in metal-insulator nanocomposites with tunneling. *Phys. Rev. B* **58**, R13375–R13378 (1998).

[18] Sarychev, A. K. & Brouers, F. New scaling for ac properties of percolating composite materials. *Phys. Rev. Lett.* **73**, 2895–2898 (1994).

[19] Qazilbash, M. M. *et al.* Mott transition in VO_2 revealed by infrared spectroscopy and nano-imaging. *Science* **318**, 1750–1753 (2007).

[20] Grannan, D. M., Garland, J. C. & Tanner, D. B. Critical behavior of the dielectric constant of a random composite near the percolation threshold. *Phys. Rev. Lett.* **46**, 375–378 (1981).

[21] van Dijk, M. A., Casteleijn, G., Joosten, J. G. H. & Levine, Y. K. Percolation in oil-continuous microemulsions. a dielectric study of aerosol ot/water/isooctane. *J. Chem. Phys.* **85**, 626–631 (1986).

[22] Clarkson, M. T. & Smedley, S. I. Electrical conductivity and permittivity measurements near the percolation transition in a microemulsion: I. experiment. *Phys. Rev. A* **37**, 2070–2078 (1988).

[23] Clarkson, M. T. Electrical conductivity and permittivity measurements near the percolation transition in a microemulsion. ii. interpretation. *Phys. Rev. A* **37**, 2079–2090 (1988).

[24] Alexandrov, Y., Kozlovich, N., Feldman, Y. & Texter, J. Dielectric spectroscopy of cosurfactant facilitated percolation in reverse microemulsions. *J. Chem. Phys.* **111**, 7023–7028 (1999).

[25] Pecharromán, C. & Moya, J. S. Experimental evidence of a giant capacitance in insulator–conductor composites at the percolation threshold. *Adv. Mater.* **12**, 294–297 (2000).

[26] Pecharromán, C., Esteban-Betegón, F., Bartolomé, J. F., López-Esteban, S. & Moya, J. S. New percolative batio3–ni composites with a high and frequency-independent dielectric constant ($\varepsilon_r \approx 80000$). *Adv. Mater.* **13**, 1541–1544 (2001).

[27] Nan, C.-W., Shen, Y. & Ma, J. Physical properties of composites near percolation. *Ann. Rev. Mater. Res.* **40**, 131–151 (2010).

[28] Berthier, S., Peiro, J., Fagnent, S. & Gadenne, P. Infrared absorption of granular metal films in the percolation range. *Physica A* **241**, 1 – 5 (1997).

[29] Hövel, M., Gompf, B. & Dressel, M. Dielectric properties of ultrathin metal films around the percolation threshold. *Phys. Rev. B* **81**, 035402 (2010).

[30] Hövel, M., Gompf, B. & Dressel, M. Electrodynamics of ultrathin gold films at the insulator-to-metal transition. *Thin Solid Films* **519**, 2955 – 2958 (2011).

[31] De Zuani, S., Peterseim, T., Berrier, A., Gompf, B. & Dressel, M. Second harmonic generation enhancement at the percolation threshold. *Applied Physics Letters* **104**, 241109 (2014).

[32] De Zuani, S. *et al.* Suppressed percolation in nearly closed gold films. *ACS Photonics* **3**, 1109–1115 (2016).

[33] Abdel-Jawad, M. *et al.* Anomalous dielectric response in the dimer mott insulator $\kappa-(\text{BEDT-TTF})_2\text{Cu}_2(\text{CN})_3$. *Phys. Rev. B* **82**, 125119 (2010).

[34] Pinterić, M. *et al.* Anisotropic charge dynamics in the quantum spin-liquid candidate $\kappa-(\text{BEDT-TTF})_2\text{Cu}_2(CN)_3$. *Phys. Rev. B* **90**, 195139 (2014).

[35] Pinterić, M. *et al.* What is the origin of anomalous dielectric response in 2d organic dimer mott insulators κ-(bedt-ttf)$_2$Cu[N(CN)$_2$]Cl and $\kappa-(\text{BEDT-TTF})_2\text{Cu}_2(CN)_3$. *Physica B* **460**, 202 – 207 (2015).

[36] Tomić, S. & Dressel, M. Ferroelectricity in molecular solids: a review of electrodynamic properties. *Rep. Prog. Phys.* **78**, 096501 (2015).

[37] Sasaki, S., Iguchi, S., Yoneyama, N. & Sasaki, T. X-ray irradiation effect on the dielectric charge response in the dimer–mott insulator $\kappa-(\text{BEDT-TTF})_2\text{Cu}_2(CN)_3$. *J. Phy. Soc. Jpn.* **84**, 074709 (2015).

[38] Cross, L. E. *Relaxor ferroelectrics*, 131–155 (Springer-Verlag, Berlin, Heidelberg, 2008).

[39] Mott, N. *Metal-insulator transitions* (Taylor & Francis, 1990), 2 edn.

[40] Pustogow, A. *et al.* (2020). To be published.

[41] Stroud, D. Generalized effective-medium approach to the conductivity of an inhomogeneous material. *Phys. Rev. B* **12**, 3368–3373 (1975).

[42] Stroud, D. & Pan, F. P. Self-consistent approach to electromagnetic wave propagation in composite media: Application to model granular metals. *Phys. Rev. B* **17**, 1602–1610 (1978).

[43] Choy, T. C. *Effective medium theory: Principles and applications* (Oxford University Press, Oxford, 2015), 2nd ed. Edn.

[44] Georges, A., Kotliar, G., Krauth, W. & Rozenberg, M. J. Dynamical mean-field theory of strongly correlated fermion systems and the limit of infinite dimensions. *Rev. Mod. Phys.* **68**, 13–125 (1996).

[45] Economou, E. *Green's functions in quantum physics* (Springer-Verlag, Berin, 2006), 3 edn.

[46] Letfulov, B. M. & Freericks, J. K. Dynamical mean-field theory of an Ising double-exchange model with diagonal disorder. *Phys. Rev. B* **64**, 174409 (2001).